A Triangulated Vortex Method for the Axisymmetric Euler Equations

Michael Carley

Department of Mechanical Engineering, University of Bath, Bath BA2 7AY, United Kingdom
E-mail: m.j.carley@bath.ac.uk

A new method is presented for the prediction of unsteady axisymmetric inviscid flows. By combining a triangulated vortex approach with a novel evaluation technique for the Biot–Savart integrals, a Lagrangian vortex method is developed which eliminates the singularities usually present in axisymmetric methods, without recourse to normalizations or other approximations. Furthermore, the computational effort scales as the number of control points N and, in the large N limit, depends only on the order of quadrature employed. The accuracy and computational effort are assessed by comparison with the velocity field of a Gaussian core vortex ring and the use of the technique is illustrated by computation of the motion of Norbury rings and of vortex ring pairing. © 2002 Elsevier Science (USA)

Key Words: vortex methods; Euler equations; triangular mesh.

1. INTRODUCTION

Since their introduction, Lagrangian vortex methods have been developed into powerful techniques for the prediction of unsteady incompressible flows. From Rosenhead's initial point vortex model [22] (and see also Low [13]) to the work of Chorin [3] and Christiansen [4], considerable progress has been made in developing methods for the prediction of vorticity dynamics in two and three dimensions. The increasing popularity of such methods is due to their conceptual simplicity and to their computational efficiency.

Lagrangian vortex methods work by discretizing a flow into regions of vorticity which are convected at the local fluid velocity, modeling the development of a flow by calculating the velocity induced on each vortex element by all of the others. Since the flow is characterized uniquely by the vorticity, this is a valid approach to the solution of the fluid dynamical equations. The method is conceptually appealing, being based on well-understood and easily visualized interactions. It is also, at least in principle, easily implemented: an initial vorticity distribution is discretized into some set of control points and the velocities of these control points are calculated by evaluating a Biot–Savart integral over the vorticity distribution.

The discretization can take a number of forms, the most common being to assume that the vorticity around each control point has a Gaussian distribution with some characteristic core size. The blobs are then made to overlap to approximate a smooth distribution of vorticity.

A number of methods have been developed which use this approach [10, 11]. For the computation of axisymmetric flows, representative examples include the calculation of vortex-generated noise [8, 12, 27], flow in burners [16] and vorticity dynamics [14, 21]. While this method is robust and efficient (especially when multipole methods are used [26]), it is not ideal for all applications.

The first difficulty is in approximating a smooth distribution of vorticity with Gaussian elements. In order to approximate the distribution, a large number of elements must be used and they must overlap sufficiently to give a smooth variation. Secondly when vortex methods are used to calculate the flow around solid surfaces, there is a difficulty in generating vorticity to satisfy the surface boundary condition. Because the Gaussian blobs have a finite radius, some of the vorticity in a blob lies inside the surface, which is clearly invalid unless some special treatment is used for surface-generated vorticity.

Recently a new approach has been developed which circumvents these problems by modeling the vorticity distribution as a set of control points which are connected by a triangular mesh. Vorticity is assumed to vary in a piecewise linear manner over each triangle and the boundary of the vorticity is clearly defined. This approach was initially developed for two-dimensional flows [23] and later extended to two-dimensional flows around solid bodies [6, 7] and to three-dimensional flows [15]. In this paper, the method will be extended to axisymmetric flows, using a novel method for the evaluation of the Biot–Savart integral, which does not directly compute element–element interactions and so reduces the computational cost of the velocity calculations. The approach also has certain numerical advantages over direct computation of element–element interactions.

A difficulty in calculating the velocity field in an axisymmetric flow is the integration of the elliptic integrals which appear in the streamfunction (6). These have a logarithmic singularity as the source point approaches the field point. The numerical integration of such a singularity is possible but time consuming. For this reason, axisymmetric vortex methods usually employ a regularization which eliminates the singularity. The approach developed in this paper removes the singularity by using a vortex disk as the basic element for integration and performing the Biot–Savart calculation without the use of elliptic integrals.

2. ANALYTICAL FORMULATION

The governing equations for an inviscid, incompressible, axisymmetric, swirl-free flow are

$$\frac{\partial \xi}{\partial t} + v_r \frac{\partial \xi}{\partial r} + v_z \frac{\partial \xi}{\partial z} = 0, \tag{1}$$

$$\frac{\partial^2 \psi}{\partial z^2} + \frac{\partial^2 \psi}{\partial r^2} - \frac{1}{r}\frac{\partial \psi}{\partial r} = -r\omega, \tag{2}$$

where r and z are the radial and axial coordinates, respectively, v_r and v_z are the corresponding velocities, ω is the azimuthal vorticity, $\xi \equiv \omega/r$, and ψ is the streamfunction. The

velocities are then

$$v_r = -\frac{1}{r}\frac{\partial \psi}{\partial z}, \tag{3}$$

$$v_z = \frac{1}{r}\frac{\partial \psi}{\partial r}. \tag{4}$$

In an inviscid flow, ξ is conserved and is transported at the local velocity (v_r, v_z). This velocity depends on the vorticity via the streamfunction

$$\psi = r \int_S \int_0^{2\pi} \frac{\omega(r_1, z_1)\cos\theta_1}{4\pi R} r_1 \, d\theta_1 \, dr_1 \, dz_1, \tag{5}$$

where

$$R = \left[r^2 + r_1^2 - 2rr_1\cos\theta_1 + (z - z_1)^2\right]^{1/2},$$

and S is the vorticity support in the $r - z$ plane (Fig. 1). Subscript 1 denotes integration coordinates.

Equation 5 can be integrated in θ_1 [5, 9],

$$\psi = \frac{1}{2\pi} \int_S \omega(r_1, z_1)(R + \rho)[K(\lambda) - E(\lambda)] \, dr_1 \, dz_1, \tag{6}$$

where K and E are complete elliptic integrals and

$$R^2 = (r - r_1)^2 + (z - z_1)^2,$$
$$\rho^2 = (r + r_1)^2 + (z - z_1)^2,$$
$$\lambda = \frac{\rho - R}{\rho + R}.$$

The basic approach to calculating an unsteady flow is then to discretize the vorticity distribution and, using the Biot–Savart integral, calculate the velocity and motion of the vorticity control points. This can be done using blob-type discretizations [14, 16, 21], as
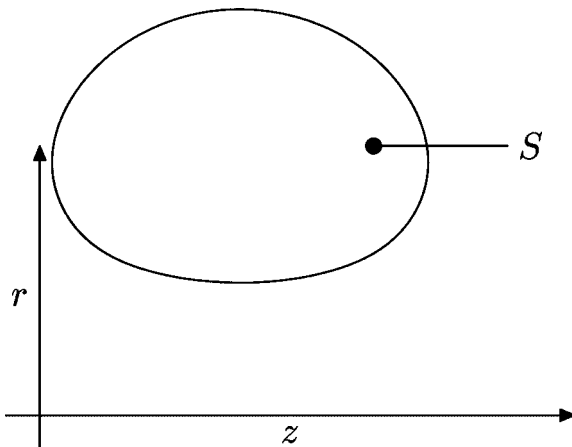

FIG. 1. Vorticity distribution in $r - z$ plane.

described above, or, as in this paper, a triangulation method [6, 7, 15, 23]. The problem then is how to evaluate the integrals.

There are two difficulties in evaluating the integral of (6). The first is one of efficiency and is common to all Lagrangian vortex methods: how to calculate the velocities at control points in a reasonable time. The second is related to the nature of the integral. As $(r_1, z_1) \rightarrow (r, z)$, there is a logarithmic singularity in the elliptic integrals. This can be handled by specialized integration schemes, but this makes coding more difficult and is inefficient. Instead a different approach has been used, which both eliminates the problem of singularities and speeds the velocity calculation.

2.1. Integration Method

The Biot–Savart integral for the axisymmetric vorticity distribution is evaluated by integrating over the triangulated vorticity distribution shown in Fig. 2a. A Gaussian quadrature
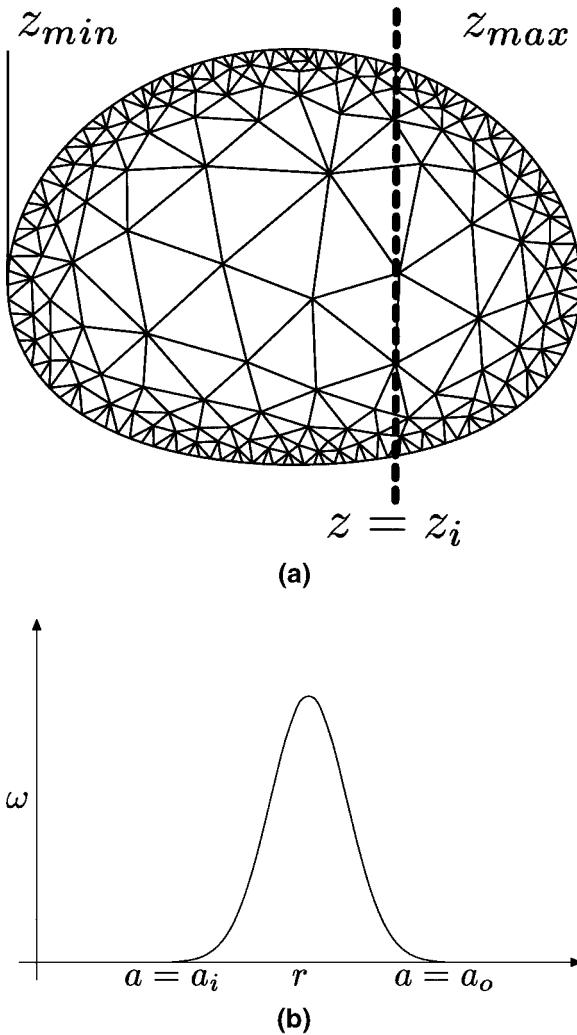
FIG. 2. Slicing the vorticity distribution to perform the Biot–Savart integral. (a) The mesh is sliced at the Gaussian quadrature points $z = z_i$; (b) the vorticity on the line $z = z_i$ is interpolated to find the vorticity distribution as a function of the radius.

is used to integrate over z, the axial coordinate. At each Gaussian quadrature point $z = z_i$, an integration in r must be performed. The first step is to "slice" the mesh in order to extract the vorticity distribution as a function of radius. Figure 2a shows the triangulation and the quadrature point $z = z_i$. Figure 2b illustrates the distribution of vorticity on the line $z = z_i$, as a function of radius. In this case, the vorticity is finite on an annulus lying between radii a_i and a_o. The slicing method is described in Section 3.1 and involves interpolating the vorticity on the mesh. When the mesh has been sliced, the vorticity can be used in the Biot–Savart integral in r to calculate the contribution of the axial station $z = z_i$ to the induced velocity at each control point of the mesh. The important point to note is that the control points are purely markers for the interpolation and have no existence as "rings" or "filaments": the Biot–Savart integral is evaluated over the triangulated region S, but no element–element interactions are ever evaluated.

2.2. The Flow Field of a Vortex Disk

The evaluation of the velocity induced by an axisymmetric distribution of vorticity is performed using a method borrowed from the acoustics of pistons [18, 19, p. 227] and rotors [1, 2]. The basic element in the calculation is a disk of azimuthal vorticity with vorticity proportional to the radius. By using such an element, general vorticity distributions can be modeled (see Section 2.3) and the boundary conditions on the axis of symmetry are satisfied. The boundary conditions on velocity and azimuthal vorticity are

$$v_r|_{r=0} = 0, \quad \left.\frac{\partial v_z}{\partial r}\right|_{r=0} = 0, \quad \omega|_{r=0} = 0. \tag{7}$$

The velocity boundary condition is satisfied because of the symmetry of the vortex disk and the vorticity boundary condition is built in to the element. The vorticity distribution is then

$$\omega(r_1, z_1) = \omega(r_1)\delta(z_1), \tag{8}$$

where $\delta(\cdot)$ is the Dirac delta function.

Figure 3 shows the coordinate system for the vortex disk, which is of radius a. Cylindrical coordinates (r, θ, z) are employed with the vortex disk placed at $z = 0$. The vorticity distribution is linear with $\omega = \Omega r_1$. The streamfunction of the disc $\psi(r, z)$ is then

$$\psi = -\Omega r \int_S \int_0^{2\pi} \frac{r_1 \cos\theta_1}{4\pi R}\delta(z_1)r_1 \, d\theta_1 \, dr_1 \, dz_1,$$

which, upon performing the integration in z_1, becomes

$$\psi = -\Omega r \int_0^a \int_0^{2\pi} \frac{r_1^2 \cos\theta_1}{4\pi R} \, d\theta_1 \, dr_1. \tag{9}$$

Differentiating, the velocity components are

$$v_r = \Omega z \int_0^a \int_0^{2\pi} \frac{\cos\theta_1}{4\pi R^3} r_1^2 \, d\theta_1 \, dr_1 \tag{10}$$
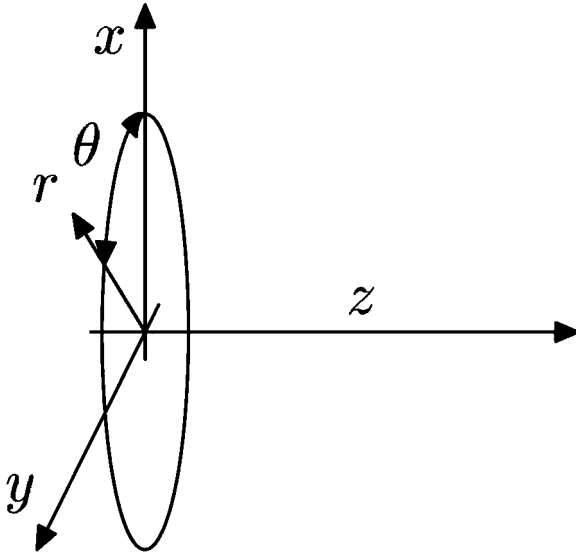
FIG. 3. Coordinate system for a vortex disk.

and

$$v_z = -\Omega \int_0^a \int_0^{2\pi} \frac{1}{r} \frac{r_1^2 \cos \theta_1}{4\pi R} - \frac{r - r_1 \cos \theta_1}{4\pi R^3} r_1^2 \cos \theta_1 \, d\theta_1 \, dr_1. \tag{11}$$

All lengths are now nondimensionalized on the disk radius a and the integrals are rewritten as

$$\psi = \Omega a^3 \Psi, \quad v_r = \Omega a V_r \quad \text{and} \quad v_z = \Omega a V_z,$$

where

$$\Psi = -\frac{r}{2} \int_0^1 \int_0^{2\pi} \frac{r_1^2 \cos \theta_1}{2\pi R} \, d\theta_1 \, dr_1, \tag{12}$$

$$V_r = \frac{z}{2} \int_0^1 \int_0^{2\pi} \frac{r_1^2 \cos \theta_1}{2\pi R^3} d\theta_1 \, dr_1, \tag{13}$$

and

$$V_z = -\frac{1}{2} \int_0^1 \int_0^{2\pi} \frac{1}{r} \frac{r_1^2 \cos \theta_1}{2\pi R} - \frac{r - r_1 \cos \theta_1}{2\pi R^3} r_1^2 \cos \theta_1 \, d\theta_1 \, dr_1. \tag{14}$$

The nondimensional integrals can now be evaluated numerically using a coordinate transformation introduced in rotor acoustics [1, 2] and previously in piston theory [18, 19]. The method was originally developed to allow numerical integrations to be performed more quickly, but its primary use here is the elimination of the singularities introduced by the use of elliptic integrals in (12)–(14). First the (r_1, θ_1) coordinates are transformed to the (r_2, θ_2) system shown in Fig. 4:

$$r_1 \cos \theta_1 = r + r_2 \cos \theta_2,$$
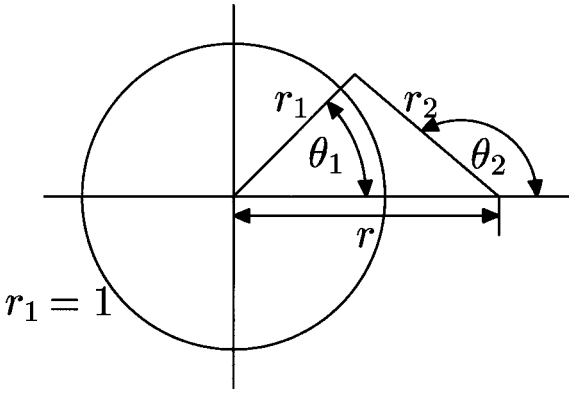$$r_1 \, dr_1 \, d\theta_1 = r_2 \, dr_2 \, d\theta_2.$$

FIG. 4. Transformed coordinate system for vortex disk integrals.

Under this transformation, the integrals of (12)–(14) are rewritten as

$$\Psi = \frac{r}{2} \int_{r_2} \left(\frac{r}{R} J_0(r, r_2) + \frac{r_2}{R} J_1(r, r_2) \right) r_2 \, dr_2, \tag{15}$$

$$V_r = \frac{z}{2} \int_{r_2} \frac{rr_2}{R^3} J_0(r, r_2) + \frac{r_2^2}{R^3} J_1(r, r_2) \, dr_2, \tag{16}$$

and

$$V_z = \frac{1}{2} \int_{r_2} \frac{r_2}{R} J_0(r, r_2) + \left(\frac{r_2^2}{rR} + \frac{rr_2^2}{R^3} \right) J_1(r, r_2) + \frac{r_2^3}{R^3} J_2 \, dr_2, \tag{17}$$

where

$$J_i(r, r_2) = \frac{1}{2\pi} \int_{\theta_2^{(0)}}^{2\pi - \theta_2^{(0)}} \cos^i \theta_2 \, d\theta_2. \tag{18}$$

The limits of integration $\theta_2^{(0)}$ depend on r and r_2, i.e.,

$$\theta_2^{(0)} = \cos^{-1} \frac{1 - r^2 - r_2^2}{2rr_2},$$

which is the value of θ_2 at which a circle of radius r_2 with center at $(r, 0)$ intersects the unit circle centered at the origin.

The function J_i can be evaluated analytically:

$$J_0 = \frac{\pi - \theta_2^{(0)}}{\pi}, \tag{19}$$

$$J_1 = -\frac{\sin \theta_2^{(0)}}{\pi}, \tag{20}$$

and

$$J_2 = \frac{\pi - \theta_2^{(0)}}{2\pi} - \frac{\sin 2\theta_2^{(0)}}{4\pi}. \tag{21}$$

When $r < 1$ and $r_2 < 1 - r$, $\theta_2^{(0)} = 0$ and $J_1 \equiv 0$.

The limits on r_2 depend on the value of r. The integral for Ψ (and similarly V_r and V_z) can be decomposed:

$$
\begin{aligned}
\Psi &= \Psi^{(1)}, & r > 1 - r, \\
\Psi &= \Psi^{(1)} + \Psi^{(2)}, & r \le 1 - r.
\end{aligned}
$$

The integral $\Psi^{(1)}$ is always evaluated and is given by

$$
\Psi^{(1)} = \frac{r}{2} \int_{|r-1|}^{r+1} \left(\frac{r}{R} J_0(r, r_2) + \frac{r_2}{R} J_1(r, r_2) \right) r_2 \, dr_2. \tag{22}
$$

This is evaluated numerically. When $r \le 1$, the contribution from $\Psi^{(2)}$ must be included and can be evaluated analytically. When $r < 1$, $r_2 < 1 - r$, $J_0 \equiv 1$, $J_1 \equiv 0$, and $J_2 \equiv 1/2$, so that

$$
\Psi^{(2)} = \frac{r^2}{2} \int_0^{1-r} \frac{r_2}{R} \, dr_2,
$$

yielding

$$
\Psi^{(2)} = \frac{r^2}{2} (R_2 - z), \tag{23}
$$

with

$$
R_2 = [(1 - r)^2 + z^2]^{1/2}.
$$

The equivalent results for the velocity integrals are then

$$
\begin{aligned}
V_r^{(2)} &= \frac{z}{2} \int_0^{1-r} \frac{r r_2}{R^3} \, dr_2 \\
&= -\frac{r}{2} \left(\frac{z}{R_2} - 1 \right).
\end{aligned} \tag{24}
$$

and

$$
\begin{aligned}
V_z^{(2)} &= \frac{1}{2} \int_0^{1-r} \frac{r_2}{R} + \frac{1}{2} \frac{r_2^3}{R^3} \, dr_2 \\
&= \frac{3 R_2^2 + z^2}{4 R_2} - |z|, \quad r > 0.
\end{aligned} \tag{25}
$$

For points on the axis of symmetry, $r = 0$:

$$
V_z = \frac{1}{2} \left(\frac{1 + 2z^2}{R_2} - 2|z| \right). \tag{26}
$$

Equations 24 and 25 both have finite limits as $z \to 0$, so that no special numerical treatment is needed to calculate the induced velocities near the vortex disk.

2.3. General Vorticity Distributions

The calculation of the velocity induced by a general radial distribution of vorticity is based on the result for the linear distribution derived in the previous section. The velocity induced by a disk of radius a with a linear distribution of vorticity $\omega = r_1$ is

$$aV_r = \frac{z}{4\pi} \int_0^a \int_0^{2\pi} \frac{r_1^2 \cos\theta_1}{R^3} \, d\theta_1 \, dr_1.$$

Differentiating this expression with respect to a yields

$$\frac{\partial}{\partial a}(aV_r) = \frac{z}{4\pi} \int_0^{2\pi} \frac{\cos\theta_1}{R^3} \, d\theta_1.$$

Likewise, the velocity induced by a disk with general vorticity distribution $\omega(r_1)$ is

$$v_r = \frac{z}{4\pi} \int_0^a \omega(r_1) \int_0^{2\pi} \frac{r_1 \cos\theta_1}{R^3} \, d\theta_1 \, dr_1,$$

which can be rewritten as

$$v_r = \int_0^a \frac{\omega(r_1)}{r_1} \frac{\partial}{\partial r_1}(r_1 V_r) \, dr_1.$$

Integrating by parts, the velocity induced by vorticity $\omega(r_1)$ on an annulus with inner and outer radii a_i and a_o is

$$v_r = \xi(r_1) r_1 V_r|_{a_i}^{a_o} - \int_{a_i}^{a_o} V_r \frac{\partial \xi}{\partial r_1} r_1 \, dr_1. \tag{27}$$

The equivalent result for the axial velocity is

$$v_z = \xi(r_1) r_1 V_z|_{a_i}^{a_o} - \int_{a_i}^{a_o} V_z \frac{\partial \xi}{\partial r_1} r_1 \, dr_1. \tag{28}$$

Obviously, in the special case $\omega \propto r_1$ (that of Norbury rings [17], for example), the integrals in (27) and (28) are identically zero and only the boundary of the vorticity distribution need be considered.

2.4. Multipole Expansion

Equations 27 and 28 provide a means of calculating the vorticity-induced velocities, in particular when the evaluation point is near the vorticity disk. When the velocity at a point far from the vorticity disk is to be evaluated, a multipole expansion can be used instead. The streamfunction of a vortex disk with vorticity distribution $\omega(r_1)$ is

$$\psi = -r \int_0^a \int_0^{2\pi} \omega(r_1) \frac{r_1 \cos\theta_1}{4\pi R} \, d\theta_1 \, dr_1. \tag{29}$$

Expanding $1/R$ in a power series in r_1,

$$\frac{1}{R} = \frac{1}{R_0} \sum_{q=0}^{\infty} \frac{a_q}{R_0^{2q}} \left[r_1^2 - 2rr_1 \cos \theta_1 \right]^q$$

$$= \frac{1}{R_0} \sum_{q=0}^{\infty} \frac{a_q}{R_0^{2q}} \sum_{s=0}^{q} \binom{q}{s} (-2r \cos \theta_1)^s r_1^{2q-s}, \tag{30}$$

where $R_0 = [r^2 + z^2]^{1/2}$ and a_q is the coefficient of x^q in the power series expansion of $(1 + x)^{-1/2}$.

To find the coefficient of r_1^n in the expansion of $1/R$, differentiate (30) n times and set $r_1 = 0$, i.e.,

$$\frac{1}{R} = \sum_{n=0}^{\infty} A_n r_1^n,$$

$$A_n = \sum_{q=[n/2]}^{n} \frac{a_q}{R_0^q} \binom{q}{2q-n} (-2r \cos \theta_1)^{2q-n},$$

where $[n/2]$ is the smallest integer greater than or equal to $n/2$. The streamfunction is then

$$\psi = -\frac{r}{4\pi} \sum_{n=0}^{\infty} \int_0^a r_1^n \omega(r_1) \left[\int_0^{2\pi} A_n \cos \theta_1 \, d\theta_1 \right] dr_1.$$

The integrals in θ_1 can be evaluated using the formula

$$\int_0^{2\pi} \cos^n \phi \, d\phi = 0, \quad n \text{ odd},$$

$$= \frac{\pi}{2^{n-1}} \binom{n}{n/2}, \quad n \text{ even},$$

and

$$\psi = \frac{1}{4} \sum_{n=0}^{\infty} \int_0^a r_1^{2n+2} \omega(r_1) \, dr_1 \sum_{q=0}^{2n+1} a_q \binom{2q-2n}{q-n} \binom{q}{2q-2n-1} \frac{r^{2q-2n}}{R_0^{2q+1}}. \tag{31}$$

The velocities are then calculated using the relations

$$-\frac{1}{r} \frac{\partial}{\partial z} \left(\frac{r^n}{R_0^m} \right) = \frac{mzr^{n-1}}{R_0^{m+2}}$$

and

$$\frac{1}{r} \frac{\partial}{\partial r} \left(\frac{r^n}{R_0^m} \right) = \frac{nr^{n-2}}{R_0^m} - \frac{mr^n}{R_0^{m+2}}.$$

3. NUMERICAL IMPLEMENTATION

The technique described in Section 2 has been implemented in an axisymmetric fluid dynamics code. To simplify code development, the GNU Triangulated Surface Library [20] has been used to code the triangulation and mesh slicing procedures. To speed the calculations, the unit disk velocities V_r and V_z are precomputed and an interpolation routine is used in evaluating (27) and (28) with the multipole expansion, Eq. 32, used for points which lie outside the domain where the velocities have been computed. Because V_r is antisymmetric and V_z symmetric, in z, the integrals need be precomputed only for positive z.

To start the computation, the initial vorticity distribution is meshed (using the TRIANGLE code [24]) to generate the control points. At each time step, the control points are triangulated, using the GNU Triangulated Surface library [20], and the triangulation is sliced to evaluate the velocity integrals. Integration is performed using Gaussian quadrature. At each Gaussian quadrature point $z = z_i$, the mesh is sliced to provide the data for the evaluation of (27) and (28) at each control point. Stating the procedure explicitly:

ALGORITHM 1.
Triangulate the control points.
Generate the bounding box tree for the triangles.
For each Gaussian quadrature point $z = z_i$:
Slice the vorticity distribution (Section 3.1):
    Select bounding boxes which straddle $z = z_i$.
    Find the intersection of the bounded triangle with $z = z_i$.
    Sort the intersection points and discard duplicates.
**Evaluate** the velocity contribution for each control point.

3.1. Mesh Slicing

The application of the method described in this paper to the calculation of the velocity induced by the vorticity distribution requires the extraction of vorticity data on slices of constant z. Fortunately, this operation can be performed efficiently using axis-aligned bounding boxes. After the control points have been triangulated, a bounding box tree is generated which provides an efficient means of finding triangles which are intersected by a plane $z = z_i$. Figure 5 shows the procedure applied to part of a simple mesh. The mesh triangles are shown in Fig. 5a, along with the line $z = z_i$. In Fig. 5b, the bounding boxes for the triangles are shown (but not the higher level bounding boxes), with the boxes which straddle $z = z_i$ shown in bold. Finally, Fig. 5c shows the triangles and bounding boxes, with the intersection points of $z = z_i$ and the triangles indicated. The vorticity at each point is calculated by linear interpolation between the two points of the edge which intersects $z = z_i$.

After the points of intersection are found, they are sorted in order of increasing r. Because of the manner in which the points are found, there are a number of duplicates which must be removed from the list. The final result is a sorted list of points which define the vorticity distribution at the axial station $z = z_i$.

3.2. Meshing Considerations

The meshing and remeshing of the vorticity distribution are of some importance in a triangulated vortex method [6, 7, 23], especially in the axisymmetric case, which has
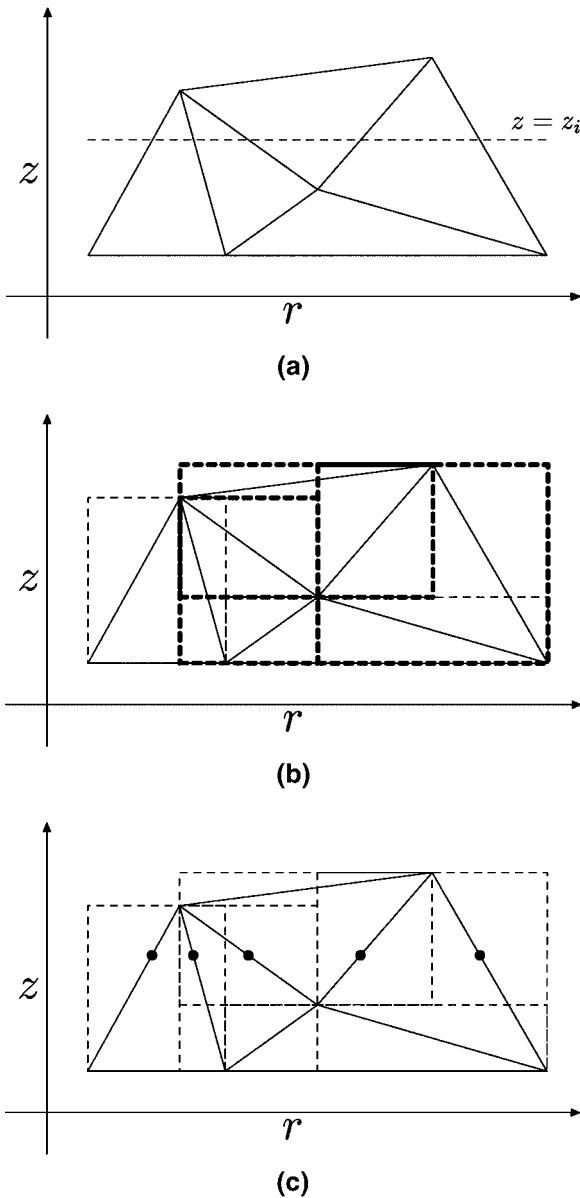
FIG. 5.   Slicing the meshed vorticity to find a radial vorticity distribution. (a) Triangulation and line $z = z_i$; (b) bounding boxes, with boxes straddling $z = z_i$ shown bold; (c) triangulation with points on edges intersecting $z = z_i$, shown as solid circles.

features not seen in the two-dimensional problem. In Section 5.2, the interaction of two initially identical vortex rings is examined. In the plane case, regions of vorticity interact symmetrically, but in the axisymmetric problem, there is large deformation and the two rings merge. This large deformation leads to intense distortion of the control point distribution and of the triangulation, leading to inaccurate interpolation of vorticity on the mesh.

Figure 6 shows an example of the problems to be overcome. Figure 6a shows an initial mesh for the problem in Section 5.2. This mesh, generated using TRIANGLE [24], has a smooth distribution of well-formed triangles. Figure 6b shows the same mesh at
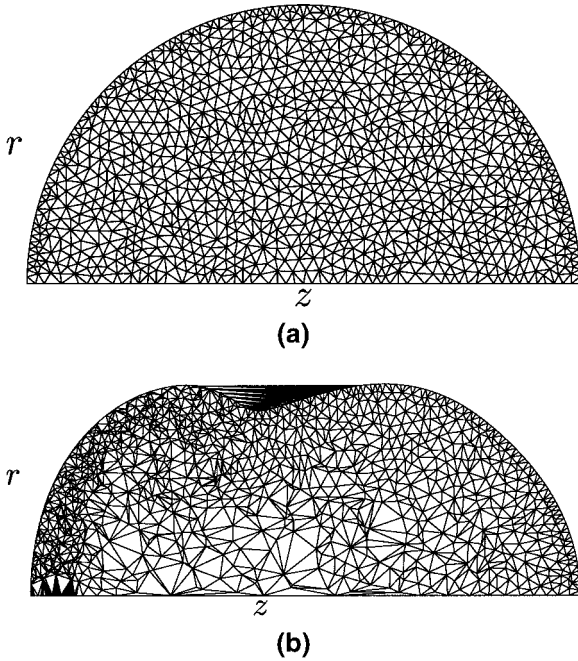
FIG. 6.   Mesh distortion. (a) Initial mesh; (b) mesh distortion at $t = 6$ (see Fig. 11d).

a nondimensional time $t = 6$, which corresponds to the results of Fig. 11d. No attempt has been made to regulate the mesh quality and the deterioration is obvious. The first effect is that the triangles of the mesh vary in size and, especially, in quality. This is mainly due to the nonuniform flow, which causes strong distortion on the left-hand side and very little distortion on the right-hand side of the mesh. As control points move with the flow, points which were initially close together diverge and the associated triangulation loses quality.

A second effect is visible at the top of the mesh. As the vortex rings interact, they draw fluid (i.e., control points) into the region between them (see Fig. 11). This causes part of the boundary of the mesh to become concave. The triangulation is bounded by the convex hull of the control points so that spurious triangles are generated on the mesh boundary. The vorticity in this region is very small, so these triangles do not cause large errors, but in other problems this might not be true. It should be noted that the drawing in of the control points is a real physical effect, so denoting certain points as boundary nodes and requiring the triangulation to conform to them is not a valid solution to the problem. In this case, the problem is solved by meshing a large domain so that the vorticity near the boundaries is very small and the spurious triangles do not introduce a large error in the interpolated vorticities.

To maintain the mesh quality, however, a different approach is required. The method adopted here is to set a maximum and a minimum edge length in the triangulation. Edges which exceed a maximum length as they stretch are split by having a new control point inserted at their midpoints. Edges which fall below a minimum length are collapsed and their endpoints merged. The effect of setting a maximum length is to maintain resolution in the mesh. Setting a minimum length has the effect, first, of ensuring that the number of control points does not become too great and, second, of maintaining the quality of triangles in the mesh: setting a maximum and minimum edge length imposes a *de facto* aspect ratio on triangles.

4. ALGORITHM PERFORMANCE

The accuracy and speed of the velocity evaluation method have been evaluated by comparison with the computed velocity field of a Gaussian core vortex ring. A problem in testing the method is that the axisymmetric problem does not have the wide range of analytical solutions available for the two-dimensional problem. An obvious reference would be Hill's spherical vortex, which has been used as a test case for other axisymmetric vortex problems [14, 15], as have the related Norbury rings [17]. These are unsuitable as general test cases for the method of this paper, however, because they are based on a vorticity distribution $\omega \propto r$, precisely that which is used in the development of the present technique. This means that such a problem would not provide a full test of all the elements of the evaluation technique. For this reason, a Gaussian core vortex has been chosen, as it has a peaked vorticity distribution and a large variation in vorticity magnitude, features which must be handled correctly by the evaluation method.

The velocities are calculated by differentiation of (5), i.e.,

$$v_r = -\frac{1}{2\pi r} \iint \left[\left(\frac{\partial R}{\partial z} + \frac{\partial \rho}{\partial z} \right) K - \left(\frac{1}{1-\lambda} \frac{\partial R}{\partial z} + \frac{1}{1+\lambda} \frac{\partial \rho}{\partial z} \right) E \right] \omega \, dr_1 \, dz_1, \quad (32a)$$

$$v_z = \frac{1}{2\pi r} \iint \left[\left(\frac{\partial R}{\partial r} + \frac{\partial \rho}{\partial r} \right) K - \left(\frac{1}{1-\lambda} \frac{\partial R}{\partial r} + \frac{1}{1+\lambda} \frac{\partial \rho}{\partial r} \right) E \right] \omega \, dr_1 \, dz_1, \quad (32b)$$

where the dependence of the elliptic integrals on λ and of ω on (r_1, z_1) has been suppressed for clarity. The velocities are calculated numerically by integration of (33) using an analytically specified vorticity distribution corresponding to a Gaussian core ring of unit radius

$$\omega(r_1, z_1) = \frac{e^{-R_0^2/\sigma^2}}{\pi \sigma^2}, \quad (33)$$

$$R_0 = \left[(r_1 - 1)^2 + z_1^2 \right]^{1/2}. \quad (34)$$

In order to numerically integrate (33), the logarithmic singularity in the elliptic integral K must be handled correctly. This is done by transforming the coordinates to center on the evaluation point (r, z):

$$r_1 = r + R \cos \phi, \quad z_1 = z + R \sin \phi, \quad dr_1 \, dz_1 = R \, dR \, d\phi. \quad (35)$$

The resulting velocity integrals are then

$$v_r = -\frac{1}{2\pi r} \int_0^{2\pi} \int_0^{R_o(\phi)} \left[\left(\frac{\partial R}{\partial z} + \frac{\partial \rho}{\partial z} \right) K - \left(\frac{1}{1-\lambda} \frac{\partial R}{\partial z} + \frac{1}{1+\lambda} \frac{\partial \rho}{\partial z} \right) E \right] \omega R \, dR \, d\phi, \quad (36a)$$

$$v_z = \frac{1}{2\pi r} \int_0^{2\pi} \int_0^{R_o(\phi)} \left[\left(\frac{\partial R}{\partial r} + \frac{\partial \rho}{\partial r} \right) K - \left(\frac{1}{1-\lambda} \frac{\partial R}{\partial r} + \frac{1}{1+\lambda} \frac{\partial \rho}{\partial r} \right) E \right] \omega R \, dR \, d\phi. \quad (36b)$$

The limits of integration vary with (r, z): the upper limit $R_o(\phi)$ varies with ϕ and was set to $R_0 + 8\sigma$. This guarantees that the region of greatest vorticity is always included in the

integration. A check was performed at each value of ϕ to ensure that the upper limit did not extend across the z-axis, i.e., that

$$r + R(\phi)\cos\phi \geq 0.$$

If this condition was violated, $R_o(\phi)$ was reduced to $-r/\cos\phi$, so the integration never extended beyond the symmetry axis.

To perform the integration of (33), the integration in R was broken into two parts, an inner region, $0 \leq R \leq R_i$, and an outer region, $R_i \leq R \leq R_o$. In the inner region, a special Gaussian quadrature [25] which correctly integrates logarithmic singularities was used, while a standard Gaussian quadrature was used in the outer region.

To apply the proposed method, the vorticity was meshed on a circle of radius 4σ centered on the core, with $\sigma = 0.1$. The mesh was not optimized for the vorticity distribution but quality and area constraints were applied. By varying the constraint on the maximum triangle area, the number of control points was changed from 161 to 4075, a range of 4.7 octaves. Velocities were calculated using Gaussian quadrature, varying the number of quadrature points used in the axial and radial directions, N_z and N_r, respectively. Calculations were performed for $N_z \times N_r$ equal to 512×512, 512×256, 256×256, 128×128, and 64×64. All computations were performed on a Pentium III personal computer.

We note that while the selected limits on R in (37) guarantee that the main region of vorticity is always included in the integration, the integration extends outside the region covered by the computational mesh for the proposed evaluation method. This means that there will automatically be some difference between the two calculation techniques, but since the vorticity which is excluded from the computational mesh is exponentially small, this difference should be negligible. Since the imposition of a computational mesh will always involve the truncation of a Gaussian vorticity distribution, such an error is, in any case, inevitable. The decision was thus taken to make the reference calculation more accurate than the new technique, in order to provide a proper test.

4.1. Computational Effort

The computational effort for the velocity evaluation can be broken up into that required for the integration proper (i.e., the Gaussian quadrature) and that required for preprocessing (control point triangulation and bounding box generation). The integration effort would be expected to scale as $N_z N_r N$, i.e., to be proportional to the number of axial quadrature points (or slices), the number of radial quadrature points, and the number of control points. For large N, this effort should dominate the computation time. Figure 7 confirms this prediction: the computational effort for each of the quadratures used asymptotes to a horizontal line and the effort, or separation between the curves, is proportional to the number of quadrature points used, in particular for $N \gtrsim 2^{10}$. The computational effort scales on the number of control points as $(N_z N_r)^{0.998}$ for $N = 4075$ and as $(N_z N_r)^{0.956}$ for $N = 161$. The preprocessing effort is thus negligible in the overall effort required for the velocity evaluation. A direct comparison with the performance of other algorithms is probably not meaningful, since the effort for the technique of this paper is always $O(N)$, rather than the $O(N^2)$ or $O(N \log N)$ performance of most other algorithms. A more meaningful comparison is the accuracy of the velocity evaluation as a function of the number of control points, discussed in the next section.
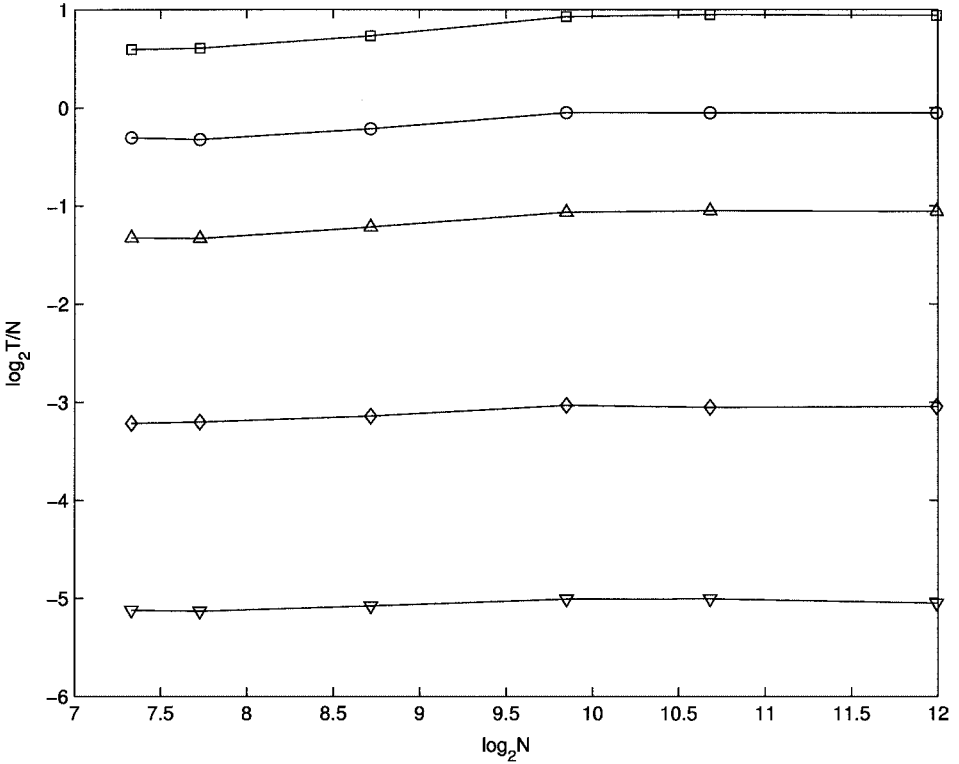
FIG. 7. Computational effort for velocity evaluation: 512×512 quadrature points, squares; 512×256 quadrature points, circles; 256×256 quadrature points, up triangles; 128×128 quadrature points, diamonds; 64×64 quadrature points, down triangles.

4.2. Accuracy

As noted above, the computational effort for the algorithm of this paper is always $O(N)$. This means that the accuracy of the method is the primary measure of quality, on two counts: the accuracy proper and the computational effort required to attain a given accuracy. Two measures of error have been considered, the root mean square error in velocity,

$$E_{\mathrm{rms}} = \left[\frac{1}{N} \sum_{i=1}^{N} \frac{(U_i - V_i)^2}{U_i^2} \right]^{1/2},$$

and, following Russo and Strain [23], the L^∞ norm of the velocity error,

$$E_v = \frac{\max_i |U_i - V_i|}{\max_i |U_i|},$$

where U and V are the velocity magnitudes calculated using (37) and the algorithm of this paper, respectively.

Figure 8 shows the two error measures as a function of number of control points (Figs. 8a and 8b) and of computation time (Figs. 8c and 8d). The first point to note is that the rms error is rather jagged and is possibly not as robust a measure of algorithm accuracy as the L^∞ norm adopted by Russo and Strain [23]. This appears to be due to small absolute errors in small velocities giving large relative errors. The L^∞ norm is thus taken as the primary
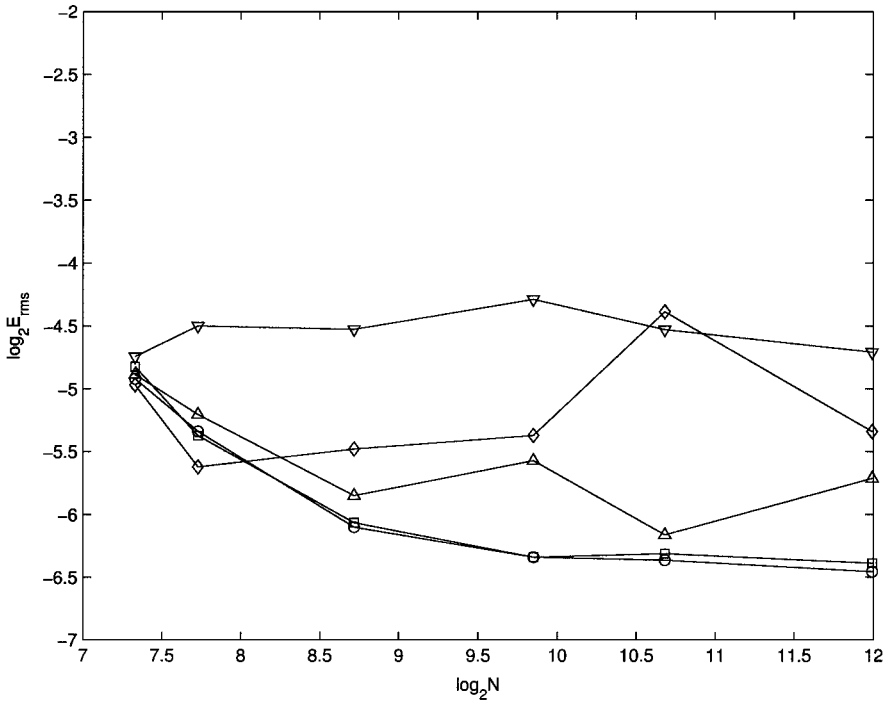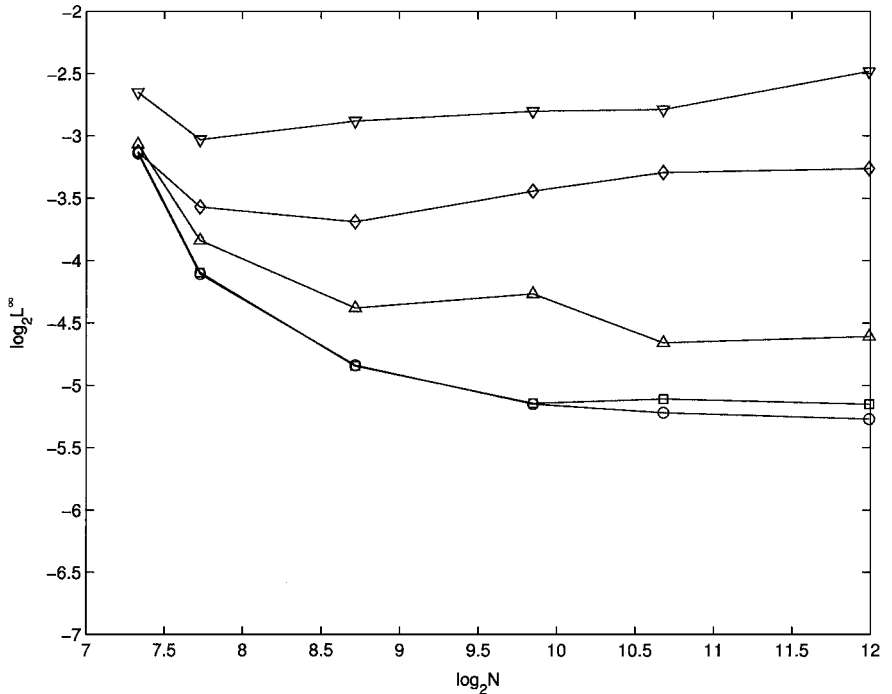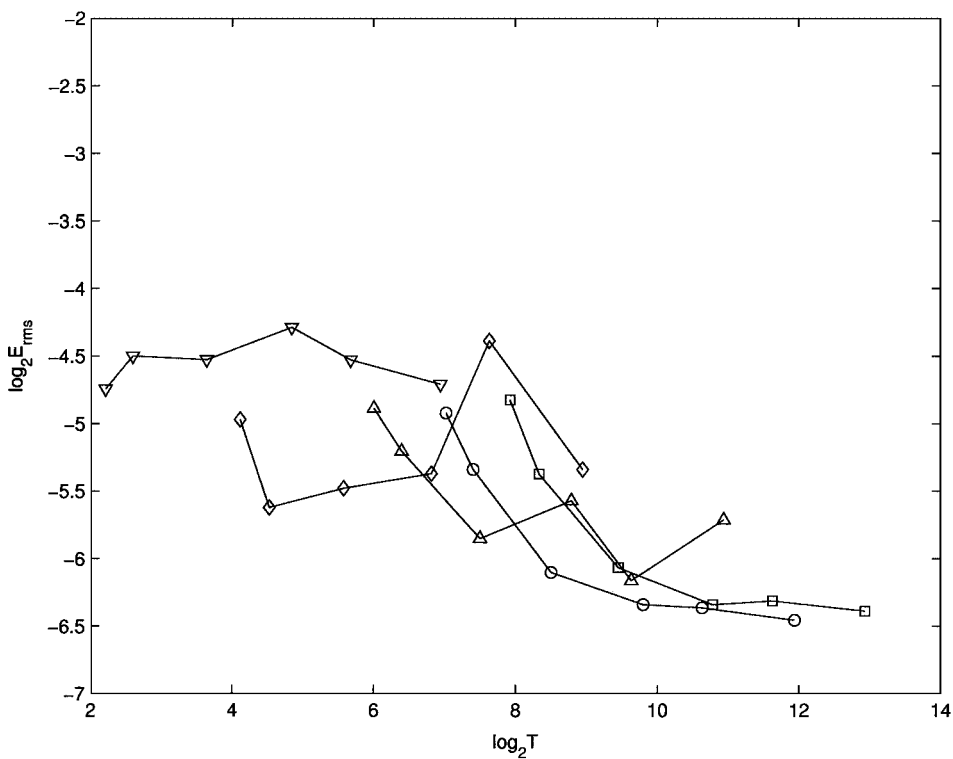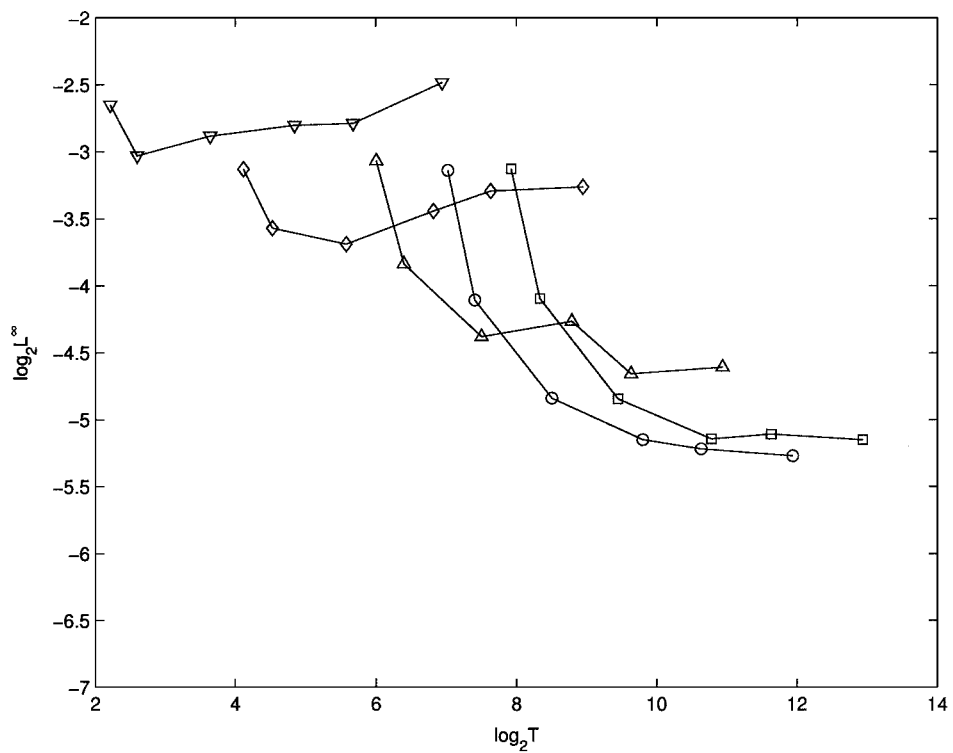
FIG. 8. Velocity error: 512 × 512 quadrature points, squares; 512 × 256 quadrature points, circles; 256 × 256 quadrature points, up triangles; 128 × 128 quadrature points, diamonds; 64 × 64 quadrature points, down triangles. (a) rms error versus number of control points; (b) L^∞ norm versus number of control points; (c) rms error versus computation time; (d) L^∞ norm versus computation time.

FIG. 8—*Continued*

measure of error. Figure 8b shows that this can be reduced with the number of quadrature points used and, for $N_z N_r > 128 \times 128$, with the number of control points. For the higher order quadratures, the error falls quite quickly before reaching a roughly constant value for $N \gtrsim 2^9$. The error in this case comes from two sources: the quadrature itself, which is of fixed order, and the interpolation error, which is a function of the mesh. We note that no error has been introduced in reformulating the problem: the equations for the velocities in Section 2.3 are exact restatements of the Biot–Savart integrals and not approximations of them. This means that any error in the computed results is due to the numerical procedures used and not to the formulation itself.

For small N, the error is dominated by the interpolation, so that the error (on both measures) is roughly independent of the number of quadrature points. As N is increased, the error is reduced as the order of the quadrature rises. The variation of the error with N is similar to that of the three-dimensional tetrahedral vorticity method of Marshall *et al.* [15, Fig. 2], where the rms error in an indirect calculation is shown to decrease rapidly with N for small N and then to level off. The rms error shown in Fig. 8a is comparable to that of [15], for the two higher order quadratures.

Figures 8c and 8d show the variation of error with computation time. Again, for the higher order quadratures, the error falls quickly with CPU time before reaching a constant value. The shape of the curves for the higher order quadratures appears to confirm the hypothesis of the source of the errors: for small N, the error depends on the interpolation or number of control points, so that increasing the number of control points has little effect above a certain threshold, while at large N, the accuracy is controlled by the number of quadrature points and the expenditure of extra computational effort results in improved accuracy.

In summary, the error depends on the number of control points N and on the order of quadrature $N_z N_r$ adopted. For small N, the error depends on N, while for large N it depends on $N_z N_r$, becoming independent of N at large N.

5. RESULTS

Two sample problems are solved to demonstrate the application of the method developed in Sections 2 and 3. The first is the calculation of the propagation velocity of steady vortex rings from the family defined by Norbury [17]. These are rings for which vorticity is proportional to radius and are thus the simplest problem to which the method of this paper applies. The second problem is the interaction of two initially identical vortex rings, a model problem for certain aspects of jet noise.

5.1. Norbury Rings

The Norbury family of vortex rings [17] is made up of vortex rings characterized by a core-size parameter α. Values of α near zero correspond to infinitesimal circular core rings, while $\alpha = \sqrt{2}$ defines Hill's spherical vortex. Both the propagation velocity and core shape depend on α and data have been given by Norbury for each of these [17], as well as for other relevant characteristics of the rings. The vorticity distribution inside the core is proportional to the radius, so that only the core boundary terms in (27) and (28) contribute to the motion. For this reason, as seen in Fig. 9, the vorticity mesh can be quite coarse. The boundary, on the other hand, must be finely discretized.

Figure 10 shows the computed propagation velocity of vortex rings with varying values of α compared to the velocities given by Norbury [17]. The match is excellent, as might be expected given the nature of the calculation method. We note that strictly speaking there is
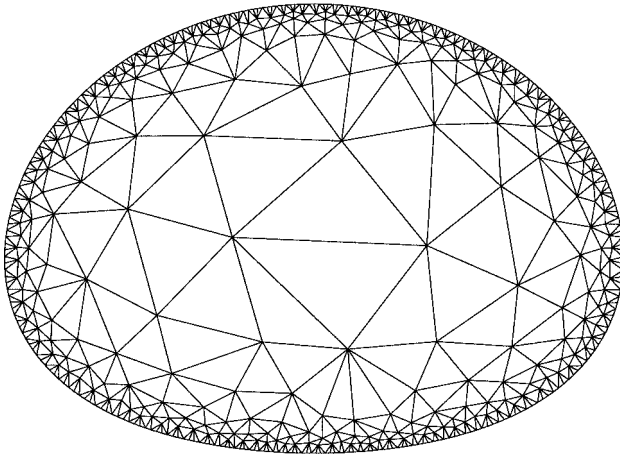
FIG. 9. Meshed Norbury ring, $\alpha = 0.6$.

no need to discretize the interior of the vortex core if the vorticity distribution is prescribed to be linear, in which case only the boundary need be described.

5.2. Pairing of Vortex Rings

The second problem to which the method of this paper has been applied is that of the interaction of two initially identical vortex rings. This has previously been studied as a model problem for noise generation by circular jets [28] and the same parameters have
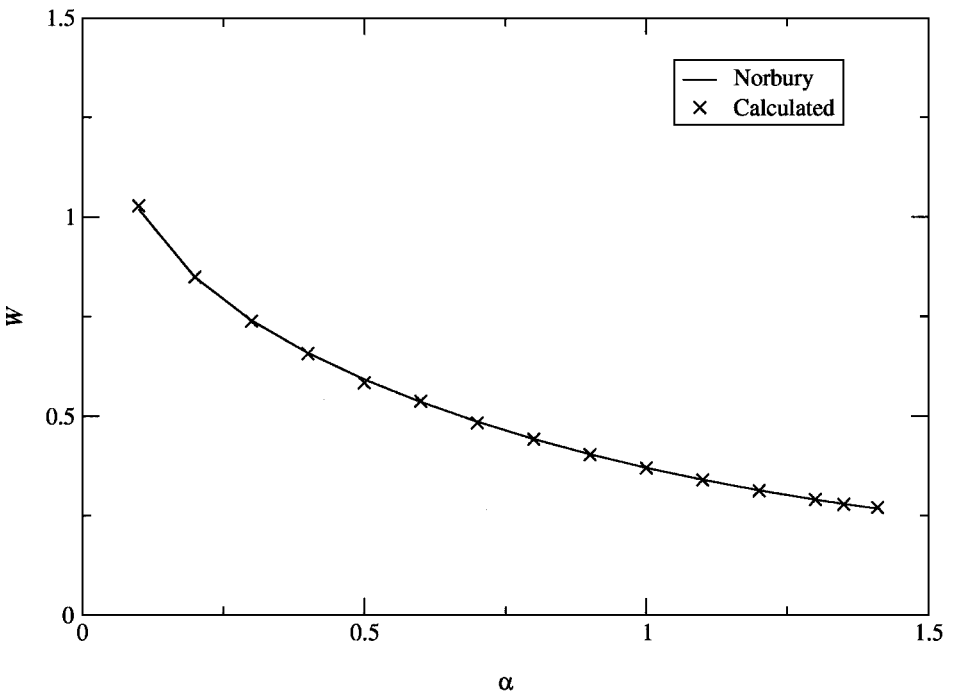
FIG. 10. Computed and theoretical velocities of Norbury rings.

been used as in the previous study. The ring cores are initially circular, with a Gaussian distribution of vorticity in the core and a core-thickness-to-ring-radius ratio of 0.3. Lengths have been nondimensionalized on ring radius and times on ring circulation. The rings are initially one radius apart. Figure 11 shows the development of the vorticity field (see also
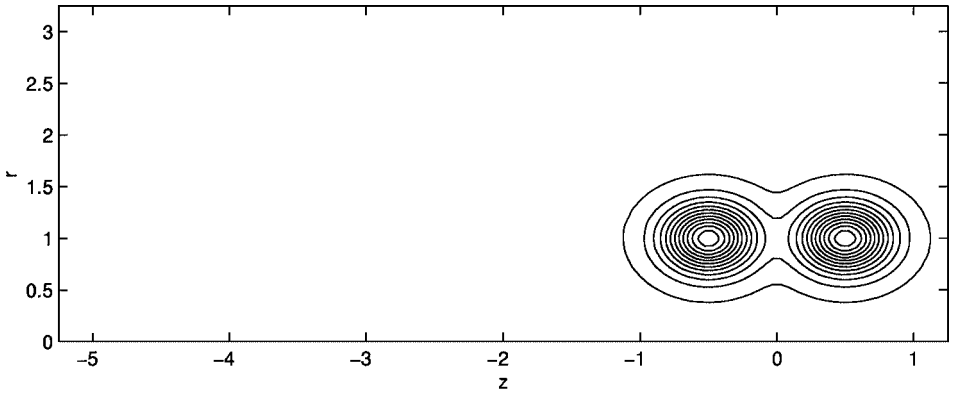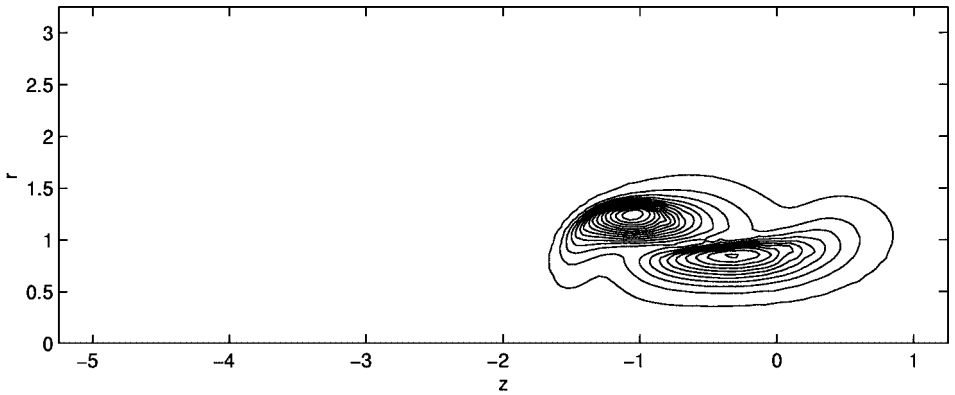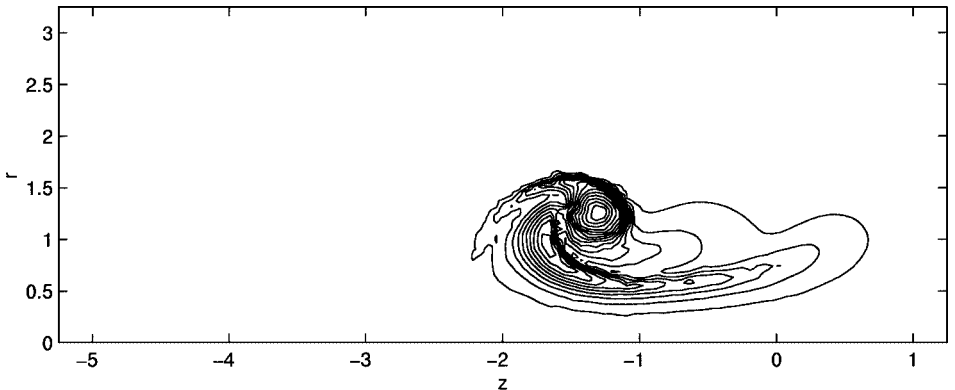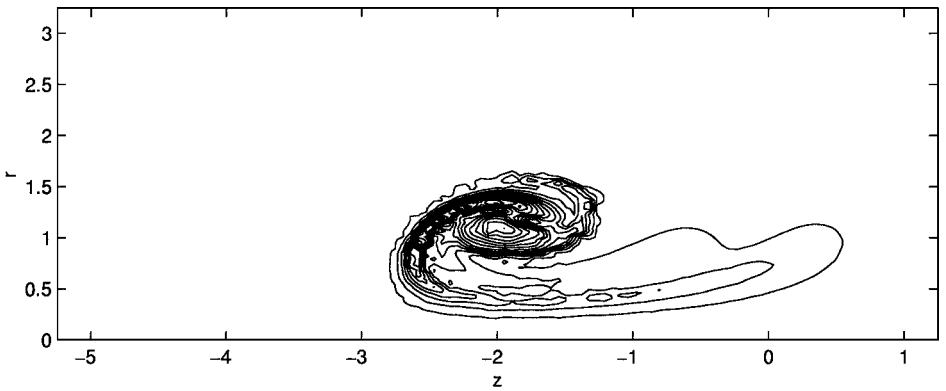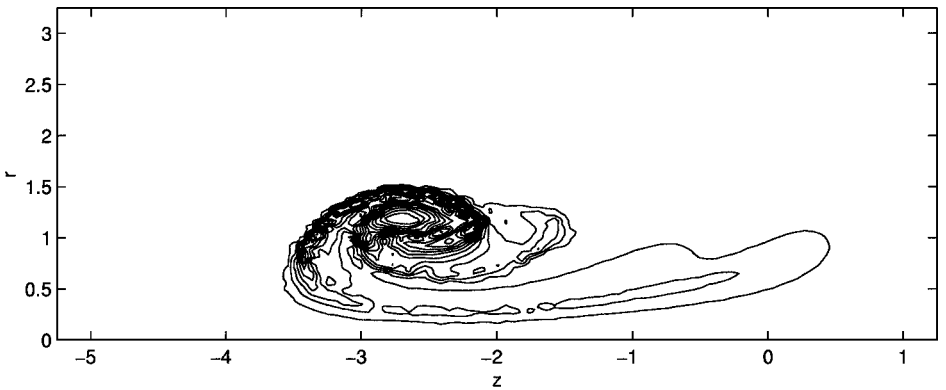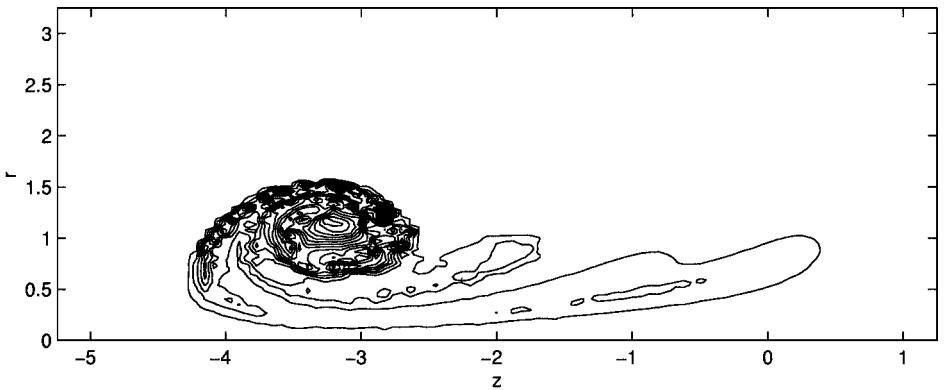

FIG. 11. Evolution of vorticity during the interaction of two identical vortex rings. (a) $t = 0$; (b) $t = 2$; (c) $t = 4$; (d) $t = 6$; (e) $t = 8$; (f) $t = 10$. The contour spacing is 0.3.

(d)

(e)

(f)

FIG. 11—*Continued*

Fig. 3 of Ref. [28]) at equally spaced nondimensional times. As t increases, the right-hand ring is pulled through the left-hand ring, which expands to "swallow" it. The core of the initially right-hand ring is wrapped around the core of the left-hand one and the two rings merge to form a single ring with a tail of weak vorticity trailing behind.
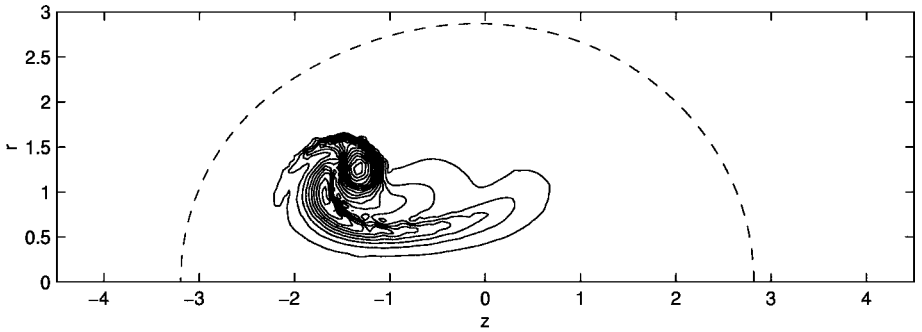
Figure 12 shows the difficulties involved in meshing this problem. These results were generated using a smaller mesh than that used for Fig. 11, to help illustrate the distortion
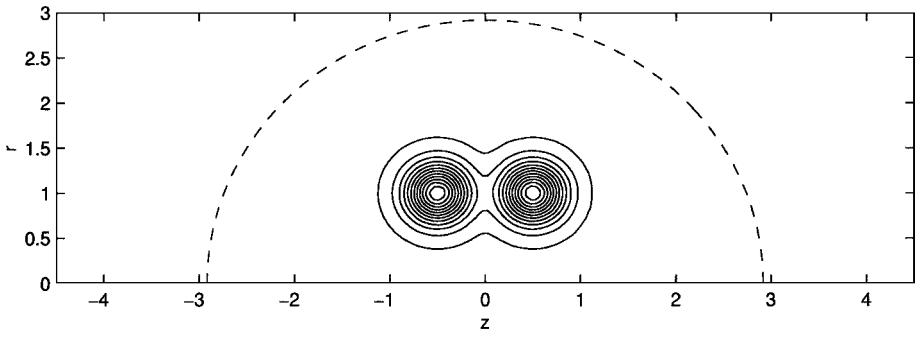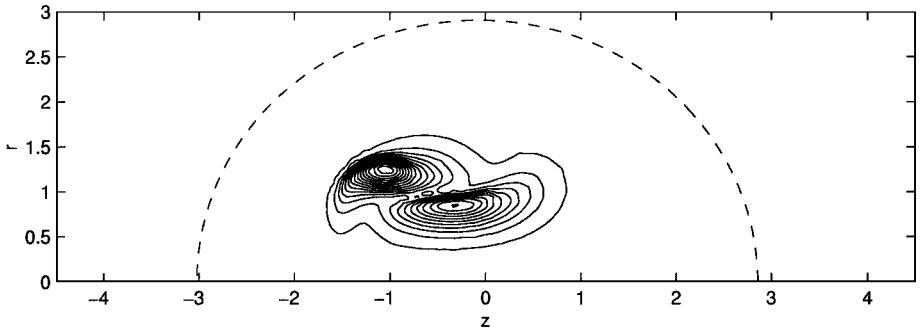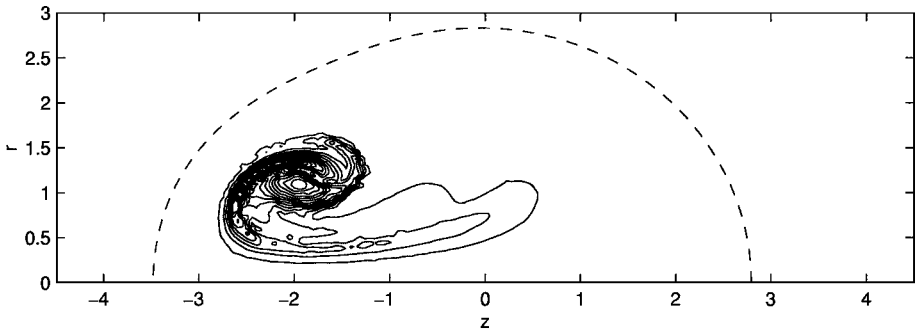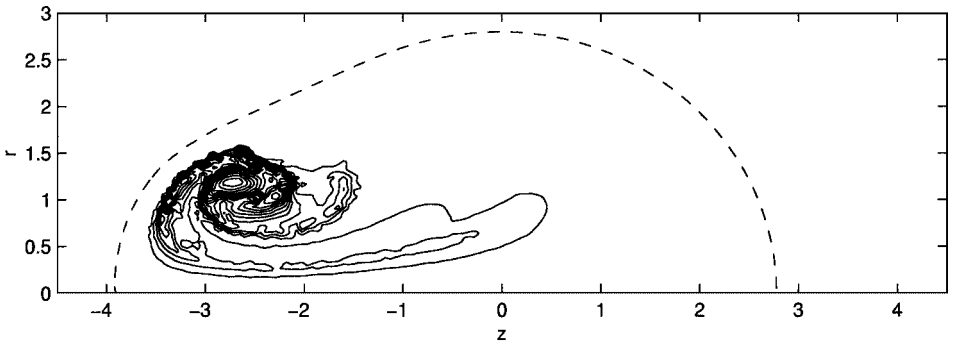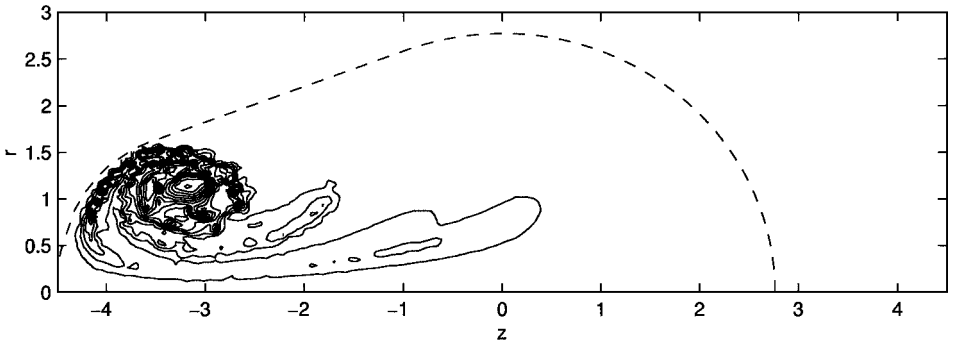
FIG. 12. Mesh distortion during ring interaction calculation: the dashed line shows the convex hull of the computational mesh. (a) $t = 0$; (b) $t = 2$; (c) $t = 4$; (d) $t = 6$; (e) $t = 8$; (f) $t = 10$.

(e)

(f)

FIG. 12—*Continued*

issue. The same results are shown for the same values of nondimensional time but with the convex hull of the control points also indicated. In the early stages of the interaction (Figs. 12a–12c), the convex hull remains semicircular, but from Fig. 12d ($t = 6$) onward, the distortion shown in Fig. 6 is obvious. As the rings interact, they begin to draw control points from the mesh boundary into the main vorticity region, causing the boundary to become concave. The convex hull then jumps over the concave region and the boundary straightens (Fig. 12f). Without some form of remeshing, this would lead to the presence of poor-quality triangles in the boundary region. Indeed, the movement of vorticity toward the mesh boundary may well be a reason for low confidence in the simulation at this point.

Finally, we note that the vorticity contours have become quite jagged by $t = 10$ in Fig. 11. The reason for this appears to be the absence of viscosity in the model, so that regions of low and high vorticity become interleaved and do not diffuse into each other. The overall vorticity distribution does, however, remain similar to that in the viscous calculations of Ref. [28].

6. CONCLUSIONS

Two previously existing numerical methods have been combined to develop a technique for the prediction of axisymmetric, inviscid, incompressible flows. By employing a tri-angulated vorticity distribution with Biot–Savart integrations performed using a method developed for rotor acoustics [1, 2], an efficient, $O(N)$, Lagrangian vortex method has been devised. In this paper, results are presented for the motion of Norbury rings [17] and for the

interaction of two initially identical circular core rings. The results are in good agreement with previously published data and demonstrate the self-adapting nature of the method and its reliability. The technique can be extended to nonaxisymmetric flows in axisymmetric domains using previously developed formulae [1, 2]. Finally, we note that the idea of "slicing" the computational mesh could also be used to develop a similar $O(N)$ approach for two-dimensional problems and provides an interesting alternative to standard multipole techniques.

REFERENCES

1. M. Carley, Sound radiation from propellers in forward flight, *J. Sound Vib.* **225**, 353 (1999), doi:10.1006/jsvi.1999.2284.

2. C. J. Chapman, The structure of rotating sound fields, *Proc. R. Soc. London Ser. A* **440**, 257 (1993).

3. A. J. Chorin, Numerical study of slightly viscous flow, *J. Fluid Mech.* **57**(4), 785 (1973).

4. J. P. Christiansen, Numerical simulation of hydrodynamics by the method of point vortices, *J. Comput. Phys.* **13**, 363 (1973).

5. I. Gradshteyn and I. M. Ryzhik, *Table of Integrals, Series and Products*, 5th ed. (Academic Press, San Diego, 1980).

6. S. A. Huyer and J. R. Grant, Computation of incipient separation via solution of the vorticity equation on a Lagrangian mesh, in *Proceedings, Second International Workshop on Vortex Flows and Related Numerical Methods* (ESAIM, Paris, France, 1996), Vol. 1, p. 109.

7. S. A. Huyer and J. R. Grant, Solution of two-dimensional vorticity equation on a Lagrangian mesh, *AIAA J.* **38**(5), 774 (2000).

8. N. W. M. Ko, R. C. K. Leung, and C. C. K. Tang, The interaction of perturbed vortex rings and its sound generation, Part II, *J. Sound Vib.* **228**(3), 511 (1999), doi:10.1006/jsvi.1999.2426.

9. H. Lamb, *Hydrodynamics*. Cambridge Mathematical Library. Cambridge University Press, Cambridge, sixth edition (1997).

10. A. Leonard, Vortex methods for flow simulation, *J. Comput. Phys.* **37**, 289 (1980).

11. A. Leonard, Computing three-dimensional incompressible flows with vortex elements, *Annu. Rev. Fluid Mech.* **17**, 523 (1985).

12. R. C. K. Leung and N. W. M. Ko, The interaction of perturbed vortex rings and its sound generation, *J. Sound Vib.* **202**(1), 1 (1997), doi:10.1006/jsvi.1996.0828.

13. A. R. Low, Postulates of hydrodynamics, *Nature* **121**(3050), 576 (1928).

14. J. S. Marshall and J. R. Grant, A Lagrangian vorticity collocation method for viscous, axisymmetric flows with and without swirl, *J. Comput. Phys.* **138**, 302 (1997), doi:10.1006/jcph.1997.5820.

15. J. S. Marshall, J. R. Grant, A. A. Gossler, and S. A. Huyer, Vorticity transport on a Lagrangian tetrahedral mesh, *J. Comput. Phys.* **161**, 85 (2000), doi:10.1006/jcph.2000.6490.

16. L. F. Martins and A. F. Ghoniem, Simulation of the nonreacting flow in a bluff-body burner; Effect of the diameter ratio, *ASME J. Fluids Eng.* **115**, 474 (1993).

17. J. Norbury, A family of steady vortex rings, *J. Fluid Mech.* **57**(3), 417 (1973).

18. F. Oberhettinger, On transient solutions of the "baffled piston" problem, *J. Res. Natl. Bur. Stand. (U.S.) B* **65**(1), 1 (1961).

19. A. D. Pierce, *Acoustics: An introduction to its physical principles and applications* (Acoustical Soc. of Am., New York, 1989).

20. S. Popinet, *GTS: GNU Triangulated Surface library*, http://gts.sourceforge.net/ (2000).

21. E. Rivoalen and S. Huberson, Numerical simulation of axisymmetric viscous flows by means of a particle method, *J. Comput. Phys.* **152**, 1 (1999), doi:10.1006/jcph.1999.6210.

22. L. Rosenhead, The formation of vortices from a surface of discontinuity, *Proc. R. Soc. London Ser. A* **134**, 170 (1932).

23. G. Russo and J. A. Strain, Fast triangulated vortex methods for the 2D Euler equations, *J. Comput. Phys.* **111**, 291 (1994), doi:10.1006/jcph.1994.1065.

24. J. R. Shewchuk, Triangle: Engineering a 2D quality mesh generator and Delaunay triangulator, in *First Workshop on Applied Computational Geometry* (ACM, Philadelphia, 1996), p. 124.

25. R. N. L. Smith, Direct Gauss quadrature formulae for logarithmic singularities on isoparametric elements, *Eng. Anal. Boundary Elements* **24**, 161 (2000).

26. J. H. Strickland and D. E. Amos, Fast solver for systems of axisymmetric ring vortices, *AIAA J.* **30**(3), 737 (1992).

27. S. K. Tang and N. W. M. Ko, Effects of a background axisymmetrical potential flow on vortex ring pairing, *J. Acoust. Soc. Am.* **104**(6), 3273 (1998).

28. R. Verzicco, A. Iafrati, G. Riccardi, and M. Fatica, Analysis of the sound generated by the pairing of two axisymmetric co-rotating vortex rings, *J. Sound Vib.* **200**(3), 347 (1997), doi:10.1006/jsvi.1996.0714.